P15R.6

SIMULATED WSR-88D MEASUREMENTS OF LOW-REFLECTIVITY EYES ASSOCIATED WITH TORNADOES

Vincent T. Wood[1], Rodger A. Brown[1], and David C. Dowell[2]
[1]NOAA, National Severe Storms Laboratory
[2]Cooperative Institute for Mesoscale Meteorological Studies, University of Oklahoma
Norman, Oklahoma

1. INTRODUCTION

In the last several years, proximity radar observations of tornadoes by mobile Doppler radars have revealed details about the three-dimensional structures of tornado vortex, including spiral bands of reflectivity surrounding a low-reflectivity eye coincident with the center of the vortex (Bluestein and Pazmany 2000; Wurman and Gill 2000; Wurman 2002; Alexander and Wurman 2005). The low-reflectivity eye typically is not visible in Weather Surveillance Radar-1988 (WSR-88D) observations because the radars are much farther away from tornadoes than are the mobile radars. Current-resolution reflectivity data collected by the WSR-88Ds have an azimuthal spacing of 1.0^{o} and range spacing of 1.0 km for reflectivity (Crum and Alberty 1993; Crum et al. 1993).

The presence of the low-reflectivity eye would be more apparent if WSR-88Ds displayed finer-resolution data. To examine this possibility, we use the high-resolution tornado numerical model of Dowell et al. (2005) and a simulated WSR-88D. Our approach involves decreasing (a) the azimuthal sampling interval from the conventional 1.0^{o} to 0.5^{o}, and (b) the range spacing from the conventional 1.0 km to 0.25 km. Simulated Doppler measurements are produced by scanning a simulated Doppler radar through the high-resolution numerical model of a mature tornado having a low-reflectivity eye coincident with the center of the tornado vortex. We compare displays of current-resolution simulated WSR-88D reflectivity signatures with displays showing simulated finer-resolution signatures.

Corresponding author address: Vincent T. Wood, National Severe Storms Laboratory, 1313 Halley Circle, Norman, OK 73069, USA. E-mail: Vincent.Wood@noaa.gov

2. APPROACH

a. Description of the model

The Dowell et al. (2005) model, which is similar to the Fiedler (1993) numerical model, simulated two-dimensional, axi-symmetric forced convection inside a closed, impermeable cylinder that rotates at a constant angular velocity (Ω). Physically, this may be viewed as a rotating updraft that draws upon ambient vertical vorticity of 2Ω, within which a tornado-like vortex develops. The governing equations in the Fielder (1993) model were solved on a uniform Cartesian grid of 25-m spacing in radial and vertical directions. The top, bottom, and lateral sides of the domain were rigid with no-slip boundary conditions. The domain was 10 km wide and 10 km tall.

Dowell et al. (2005) demonstrated how a field of precipitation particles and objects responded to steady and unsteady vortex airflows. They assumed that the particles did not coalesce or break up and did not affect air flow. Drag coefficient was isotropic which characterized the object's drag properties by its terminal fall velocity in still air.

By varying the model domain's rotation rate and the size and strength of the region of positive buoyancy, we can simulate vortices of various sizes, intensities, and types (one celled and two celled). Only one raindrop size is considered in this study. Since raindrop sizes within real tornadoes are unknown, it would be premature to conclude that a full spectrum of raindrop sizes is present. Therefore, we arbitrarily chose 1.5-mm diameter raindrops (corresponding to the terminal fall velocity of -5.4 m s^{-1}). The terminal fall velocity based on Gunn and Kinzer (1949) was assumed to be constant with height. The initial concentration of raindrops produced a uniform initial reflectivity field of 20 dBZ.

We conducted two experiments to investigate and compare Doppler radar reflectivity measurements that corresponded to two different tornado-like vortices. EXPs I and II, respectively, represent a narrow, weak vortex and a broad, strong vortex both having weak reflectivity centers.

The simulations were initialized with sold-body rotation Ω of 2x10^{-2} s^{-1} for EXP I and 1x10^{-2} s^{-1} for EXP II. The buoyancy distribution used to determine an updraft intensity along the cylinder axis was changed in both the radial (r) and vertical (z) directions by varying the maximum buoyancy (B_o), the radius of the forcing region (r_B), and the lower (z_b) and upper heights (z_t) of the forcing region. The distribution specified by Dowell et al. (2005) is given by

$$B(r,z) = B_o \cos\left(\frac{\pi r}{2r_B}\right)\sin\left[\frac{\pi(z-z_b)}{z_t - z_b}\right],$$

$$0 \le r \le r_B \text{ and } z_b \le z \le z_t, \qquad \text{(1a)}$$

$$B(r,z) = 0, \text{ otherwise.} \qquad \text{(1b)}$$

In this study, the following values were used: $B_o = 0.653$ m s^{-2}, $z_b = 1000$ m, and $z_t = 9000$ m. The radii of the forcing regions (r_B) for EXPs I and II were 500 m and 1500 m, respectively. $CAPE$ at the center of the domain is given by

$$CAPE = 2B_o\left(\frac{z_t - z_b}{\pi}\right), \qquad \text{(2)}$$

where it is approximately 3300 J kg^{-1} for both of the simulations. We used the same values for other parameters, such as diffusion coefficient and air density, that were used in the Dowell et al. (2005) simulations.

b. Doppler radar simulation

An analytical simulation of a WSR-88D was used to generate simulated mean reflectivity measurements by scanning across the tornado-like vortex (e.g., Wood and Brown 1997; Wood et al. 2001; Brown et al. 2002). The mean reflectivity factor within the radar beam was computed by averaging distributed reflectivity values within the beam that had been linearly interpolated from the three-dimensional, gridded reflectivity factors of the Dowell et al. (2005) model.

3. NUMERICAL SIMULATION RESULTS

Dowell et al. (2005) discussed how centrifuging of hydrometeors and debris rapidly produced a minimum in number concentration within the tornado-like vortex core and a maximum in the surrounding annulus. The degree of accumulation of precipitation particles in the annulus, and the rate of expansion of the annulus, increased with particle sizes.

Figure 1 presents vertical cross-sections of the 2-D velocity vectors and tangential component of air flow and model reflectivity fields in the tornado-like vortices for comparative EXPs I and II. The EXP I results are shown after 1150 s of model integration, and the EXP II results are shown after 550 s of model integration. These vortices were most intense at this time before weakening slowly at subsequent times. Differences in the vortex structures resulted from two different widths of the region of positive buoyancy, based on Eq. (1). The buoyant region was much wider in EXP II than in EXP I. Consequently, a stronger, broader rotating updraft was associated with low-altitude convergence of air parcels that originated at larger radii in EXP II (shown in Figs. 1b, d) than was associated with the smaller radii in EXP I (Figs. 1a,c). In spite of a smaller rotation rate of $\Omega = 0.01$ s^{-1} for EXP II, tangential wind speeds were higher (Fig. 1d) in EXP II owing to the greater initial circulation for parcels at the larger radii.

Strong rotation at low altitudes (Figs. 1c, d) increased pressure deficit (not shown). As the vortex continued to intensify, the pressure fell so rapidly that the upward-directed (favorable) pressure-gradient force was replaced by a downward-directed (adverse) pressure-gradient force that resulted in a central downdraft (Figs. 1a,b) at low altitudes where the vortex was most intense. The most intense stage of the vortex was followed by the formation of a strong central downdraft and temporary weakening of the vortex (not shown).

The radar reflectivity factor (e.g., Battan, 1973) is calculated from

$$Z = \sum_i n(D_i) D_i^6 , \qquad (3)$$

where $n(D_i)$ is the number of the i^{th} precipitation particles per cubic meter and D_i is the diameter (mm) of the i^{th} particle. Z is converted to logarithmic radar reflectivity in units of dBZ as follows:

$$dBZ = 10 \log_{10}\left(\frac{Z}{1\, mm^6 m^{-3}}\right), \qquad (4)$$

where the denominator refers to a reference value. Model reflectivities for EXPs I and II are presented in the last two panels of Fig. 1. The 1.5-mm diameter raindrops were lifted by the updraft, ejected from the tornado-like vortex core, and accumulated outside the core radius of maximum tangential velocity above the surface boundary layer (Dowell el al. 2005). This implies that the outward-directed centrifugal force was greater than the inward-directed pressure-gradient force. Some raindrops were carried downward by the downdraft outside the core before re-entering into the strong inflow layer in the surface boundary layer, thereby resulting in the recycling mechanism. Recycling of concentrated raindrops by the near-surface inflow and updraft was more pronounced in the broad, strong vortex (EXP II) than with the narrow, weak vortex (EXP I). Reflectivity maximum resulted mainly from concentration of rain-drops just inside the core radius of maximum tangential wind near the surface.

Dowell et al. (2005) showed that for a given hydrometeor size, different vortex sizes and strengths can affect the differences between the airflow and hydrometeor motion that developed when the hydrometeors moved in the strong gradients of the vortex's airflow. Hydrometeors centrifuged outward relative to the vortex's air and at a rate less (greater) than the air in the tangential (radial and vertical) direction. These differences are presented in Fig. 2 for the narrow, weak vortex (EXP I) and the wide, strong vortex (EXP II). As to be expected, regions of differences between the airflow and hydrometeor motion were distributed over a greater radial distance in the broad vortex than those in the narrow vortex.

In the surface boundary layer, differences between the vortex's airflow and hydrometeor motion were similar but more complicated than differences shown in the Dowell et al. (2005) experiments.

In the subsequent sections, we explore how simulated WSR-88D reflectivity signatures change with range and height when the radar scans across the numerically modeled tornadoes.

4. CURRENT- AND FINE-RESOLUTION RADAR DATA

Doppler velocity and reflectivity measurements from WSR-88Ds provide important input to forecasters as they prepare to issue short-term severe storm and tornado warnings. Current-resolution data collected by the radars have an azimuthal spacing of 1.0° and range spacing of 1.0 km for reflectivity and 0.25 km for Doppler velocity and spectrum width. The 1.0-km reflectivity data are obtained by averaging four reflectivity values that had been measured at 0.25-km range intervals.

Brown et al. (2005) tested the feasibility of improving data resolutions by employing the National Severe Storms Laboratory's test bed WSR-88D (KOUN) to collect finer-resolution data for all three radar parameters in thunderstorms using 0.5°-azimuthal spacing and 0.25-km-range spacing. They found that reflectivity signatures in severe storms were more clearly depicted with this finer-resolution data.

The azimuthal sampling interval between successive values of reflectivity, mean Doppler velocity, and spectrum width is a linear function of three radar parameters: antenna rotation rate, number of pulses transmitted and received, and time interval between pulses (Doviak and Zrnić 1993, 193-197). For a scanning radar, the antenna can move a significant fraction of the angular beamwidth during the time it takes to collect the required number of samples to make an estimate of mean Doppler velocity, reflectivity, and spectrum width within a specific resolution volume. As a consequence, the circular beam is essentially broadened in the direction of antenna rotation, producing a larger "effective" horizontal beamwidth. Through use of WSR-88D simulations in this study, the average half-power beamwidth of WSR-

88Ds is 0.89°. Thus, azimuthal resolutions of 0.5° and 1.0° produce two effective beamwidths of 1.02° and 1.39°, respectively, based on Fig. 1 of Brown et al. (2002).

In addition to the effective half-power beamwidth, the physical dimensions of the radar beam increased linearly with increasing distance from the radar. In the left panels of Fig. 3, one larger effective half-power beamwidth (1.39°) was used to process data at 0.25-km range sampling interval and one conventional azimuthal sampling interval of 1.0°. Averaging four processed reflectivity values yielded a mean reflectivity measurement at current resolution. Contributions to the mean reflectivity value from reflectivity data points outside the beamwidth (red dashed contours) were neglected.

Fine-resolution reflectivity data were processed by only one smaller effective beamwidth associated with a smaller azimuthal sampling interval of 0.5°. Thus, reflectivity measurements were recorded and displayed at 0.25-km range. They are shown in the right panels of Fig. 3.

5. EFFECTS OF TWO EFFECTIVE BEAMWIDTHS ON THE SIMULATED RADAR REFLECTIVITY SIGNATURES

a. EXP I – Narrow, weak tornado vortex

We begin our investigation of the simulated radar reflectivity signatures that corresponded to the narrow, weak tornado-like vortex (EXP I). The simulated radar reflectivity fields were computed with two effective beamwidths. We assume that the radar measurements are free of noise. Figs. 3-6 show the effects of the two beamwidths on the model low-reflectivity eye as a function of range and height. At each range, the signatures were calculated as if the radar were able to make measurements in a continuous manner in azimuth and range directions (Figs. 4 and 6). With increasing range from the radar, the lower portion of the effective beamwidth was below the ground. In this case, the mean reflectivity was computed only for that portion of the beam above the ground.

Figure 4 shows that the simulated radar reflectivity signatures became increasingly degraded with increasing distance from the radar. Degradation was due to the broadening of the radar beam with range (Fig. 3). When the diameter of the model high-reflectivity annulus was significantly larger than the nominal diameter of the radar beam (distance between the half-power points as shown in Fig. 3.), the annulus was well represented by simulated Doppler radar reflectivity measurements. On the other hand, if the diameter of the annulus was smaller than the beam diameter, radar reflectivity values were degraded because of the smearing effects of the beam.

The radar reflectivity signatures in Fig. 4 illustrate a few advantages of employing a smaller effective beamwidth and associated smaller azimuthal sampling interval to collect radar reflectivity data. The net result is improved resolution of the reflectivity signatures. At mid to large ranges from the radar, current-resolution reflectivity data became more uniform than did fine-resolution reflectivity data.

Vertical cross-sections through the lower portions of the vortices likewise show the advantages of finer-resolution radar sampling (Figs. 5 and 6). With current radar resolution, the eye was no longer detectable at ranges greater than about 50 km. However, the fine-resolution data indicate that the eye and surrounding annulus were detectable beyond 70-km range. Even though the full beamwidth was less than the width of the annulus at 10 km range for both resolutions (Figs. 5g-h), the current-resolution reflectivity field was significantly more degraded than the fine-resolution field (Figs. 6g-h) owing to averaging over 1.0 km (rather than 0.25 km) in range.

b. EXP II – Broad, strong tornado vortex

We now conduct an experiment that represents the broad, strong tornado-like vortex (EXP II). Horizontal cross-sections through the lower portions of the vortex show the advantages of finer-resolution radar sampling (Figs. 7 and 8). Between 10 and 35 km from the radar, the “knob” signature of high reflectivities (Figs. 8g,h) corresponded to a smaller annulus of high reflectivities enclosing a much smaller eye of low reflectivity (Figs. 7g,h), owing to the recycling of raindrops in the lowest few hundred meters (Dowell et al. 2005). The current-resolution knob signature was no longer detectable beyond 30-km range and then became increasingly uniform as the distance from the radar increased. The fine-resolution data, however, show that the knob signature was detectable up to about 70 km from the radar.

At a few-kilometer height above the knob signatures of high reflectivities, current- and fine-resolution radar signatures of the model low-reflectivity eye and the high-reflectivity annulus were detectable at up to about 100 km from the radar (Figs. 8a-f). However, the minimum was more pronounced in the fine-resolution data.

The advantages of finer-resolution radar sampling over current-resolution radar sampling also are illustrated in vertical cross-sections through the lower portions of the broad, strong vortices (Figs. 9 and 10). The figures reveal that current- and fine-resolution reflectivity signatures of the low-reflectivity eye and the high-reflectivity annulus were detectable at ranges up to about 70 km, but the reflectivity minima and maxima were more prominent in the fine-resolution data.

6. COMPARISON OF DOPPLER RADAR REFLECTIVITY SIGNATURES OF TWO TORNADOES

Figures 11-14 show what the simulated radar reflectivity signatures might look like as a function of range and azimuth angle on a Doppler radar reflectivity display for the two effective beamwidths and associated azimuthal sampling intervals. The radar reflectivity signatures are presented at elevation angles of 0.5^{o} and 1.5^{o} for EXPs I and II. More recognizable signatures such as low-reflectivity eyes and high-reflectivity “knobs” were associated with smaller effective beamwidths and smaller azimuthal sampling intervals. There was better sampling of the smaller-scale signatures because (a) the effective beamwidth associated with 0.5^{o} azimuthal sampling interval is narrower than that for 1.0^{o} azimuthal sampling interval and (b) there are four times the numbers of reflectivity data points in the range direction.

It is of special interest to note that strong “knob” reflectivity signatures associated with a broad strong tornado in the lower panels of Figs. 12 were produced when reflectivity maximum resulted mainly from concentration of the raindrops just inside the core radius of maximum tangential wind near the surface (Dowell et al. 2005). The knob signatures were absent in the narrow, weak tornado because the reflectivity maximum was restricted to the lowest few ten of meters. If simulated debris were included in this study, the “knob” reflectivity signatures would have been much stronger. High reflectivities in the knob signatures were similar in appearance to the 0.5^{o} KTLX WSR-88D observations of “knob” reflectivities at approximate 15-45 km from the radar during the 3 May 1999 Oklahoma City tornado (Burgess et al. 2002).

7. SUMMARY

Current- and fine-resolution WSR-88D reflectivity signatures of low-reflectivity eyes and high-reflectivity knobs associated with tornadoes were produced using the high-resolution tornado numerical model of Dowell et al. (2005) and a simulated WSR-88D. Fine-resolution data were simulated by reducing (a) the azimuthal sampling interval from the conventional 1.0^{o} to 0.5^{o}, and (b) the range sampling interval from the conventional 1.0 km to 0.25 km. As a consequence, fine-resolution displays have eight times the number of reflectivity data points.

The findings of this study indicate that fine-resolution WSR-88D measurements would increase the capability of detecting reflectivity signatures of tornadoes. There would be improved resolution of the weak-reflectivity eye at the center of the tornado out to ranges of about 100 km. For the larger, stronger tornado, the high-reflectivity knob associated with the recycling of raindrops in the lowest few hundred meters would be more prominent near the radar.

8. REFERENCES

Alexander, C. R., and J. Wurman, 2005: The 30 May 1998 Spencer, South Dakota, Storm. Part I: The structural evolution and environment of the tornadoes. *Mon. Wea. Rev.,* **133,** 72-96.

Battan, L. J., 1973: *Radar Observation of the Atmosphere*. University of Chicago Press, 324 pp.

Bluestein, H. B., and A. L. Pazmany, 2000: Observations of tornadoes and other convective phenomena with a mobile 3-

mm wavelength, Doppler radar: The spring 1999 field experiment. *Bull. Amer. Meteor. Soc.,* **131,** 2968-2984.

Brown, R. A., V. T. Wood, and D. Sirmans, 2002: Improved tornado detection using simulated and actual WSR-88D data with enhanced resolution. *J. Atmos. Oceanic Technol.,* **19,** 1759-1771.

_____, B. A. Flickinger, E. Forren, D. M. Schultz, D. Sirmans, P. L. Spencer, V. T. Wood, and C. L. Ziegler, 2005. Improved detection of severe storms using experimental fine-resolution WSR-88D measurements. *Wea. Forecasting*, **20,** 3-14.

Burgess, D. W., M. A. Magsig, J. Wurman, D. C. Dowell, and Y. Richardson, 2002: Radar observations of the 3 May 1999 Oklahoma City tornado. *Wea. Forecasting,* **17,** 456-471.

Crum, T. D., and R. L. Alberty, 1993: The WSR-88D and the WSR-88D Operational Support Facility. *Bull. Amer. Meteor. Soc.,* **74,** 1669-1687.

______, ______, and D. W. Burgess, 1993: Recording, archiving, and using WSR-88D Data. *Bull. Amer. Meteor. Soc.,* **74,** 645-653.

Dowell, D. C., C. R. Alexander, J. M. Wurman, and L. J. Wicker, 2005: Centrifuging of hydrometeors and debris in tornadoes: Radar-reflectivity patterns and wind-measurements errors. *Mon. Wea. Rev.,* **133,** 1501-1524.

Doviak, R. J., and D. S. Zrnić, 1993: *Doppler Radar and Weather Observations.* 2nd, ed., Academic Press, 562 pp.

Fielder, B. H., 1993: Numerical simulation of axisymmetric tornadogenesis in forced convection. *The Tornado: Its Structure, Dynamics, Prediction, and Hazards.* Geophys. Monogr. No. 79, Amer. Geophys. Union, 41-48.

Gunn, R., and G. D. Kinzer, 1949: The terminal velocity of fall for water droplets in stagnant air. *J. Meteor.*, **6,** 243-248.

Wood, V. T., and R. A. Brown, 1997: Effects of radar sampling on single-Doppler velocity signatures of mesocyclones and tornadoes. *Wea. Forecasting,* **12,** 928-938.

_____, _____, and D. Sirmans, 2001: Technique for improving detection of WSR-88D mesocyclone signatures by increasing angular sampling. *Wea. Forecasting,* **16,** 177-184.

Wurman, J., 2002: The multiple-vortex structure of a tornado. *Wea. Forecasting,* **17,** 473-505.

_____, and S. Gill, 2000: Finescale radar observations of the Dimmitt, Texas (2 June 1995), tornado. *Mon. Wea. Rev.,* **128,** 2135-2164.

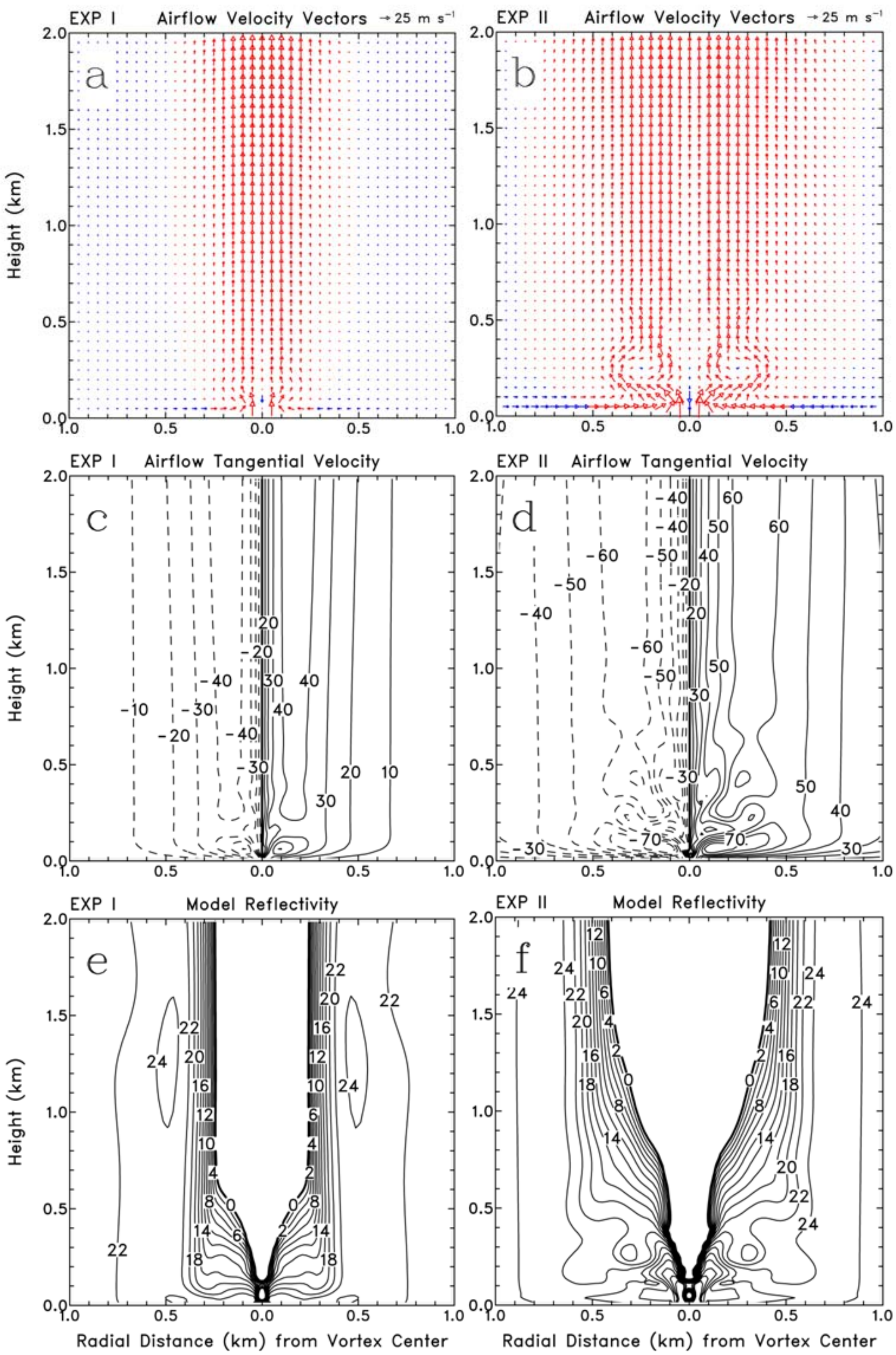

Fig. 1. Airflow (m s^{-1}) and reflectivity (dBZ) fields from Experiments I (left) and II (right) plotted in the vertical plane through the center of the vortex. (a, b) Radial and vertical airflow vectors; red (blue) vectors represent upward (downward) motion. (c, d) Airflow tangential velocity; solid (dashed) contours represent flow into (out of) the page. (e, f) Reflectivity factor computed from raindrop number concentrations; values < 0 dBZ not shown.

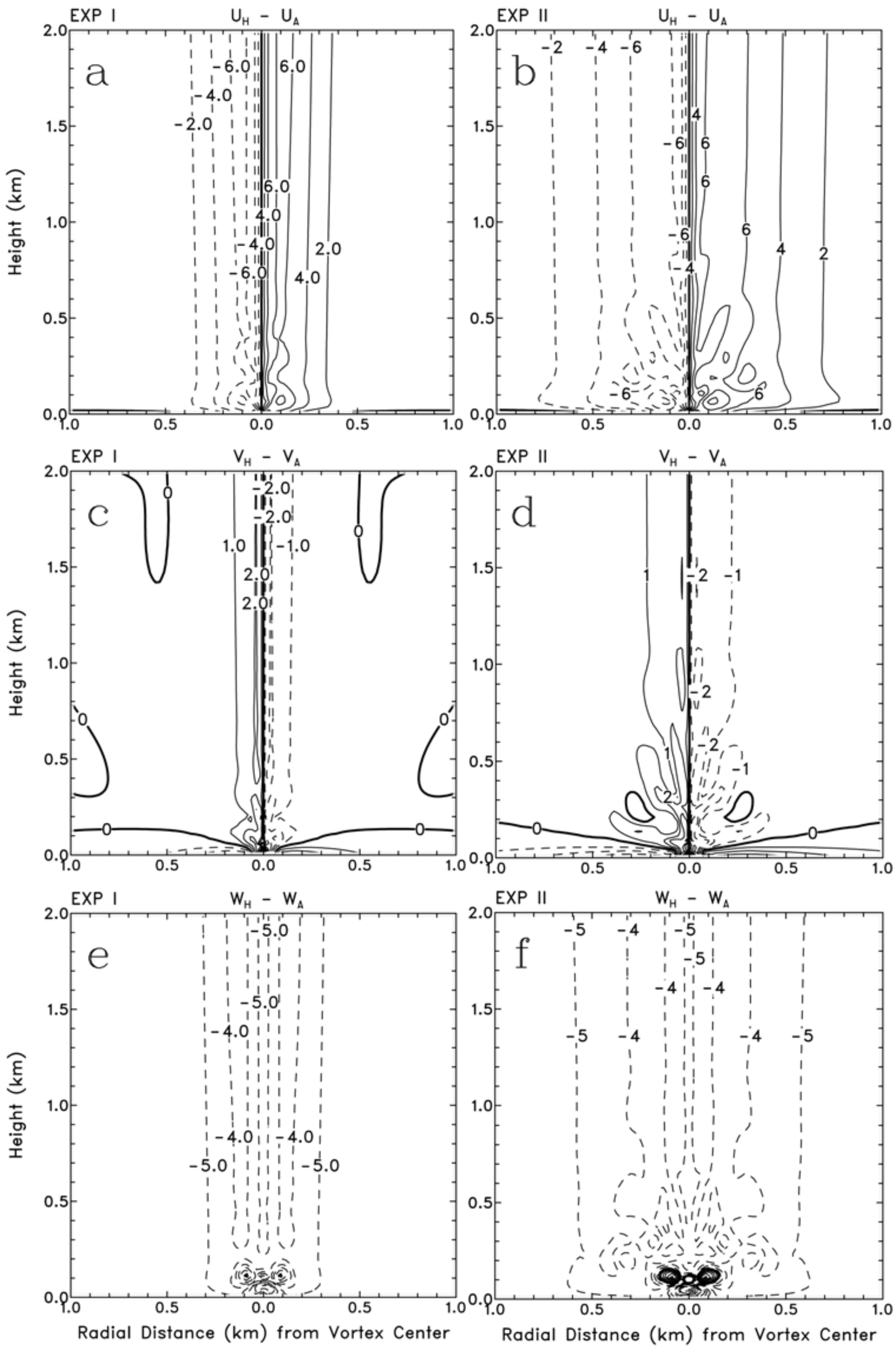

Fig. 2. Vertical plots of (a, b) radial velocity difference (u_H - u_A), (c, d) tangential velocity difference (v_H - v_A), and (e, f) vertical velocity difference (w_H - w_A) for EXPs I and II. Subscripts H and A refer to hydrometeor and airflow, respectively. Thin solid (dashed) contours represent positive (negative) values in m s^{-1}. Thick solid contour of 0 m s^{-1} is indicated.

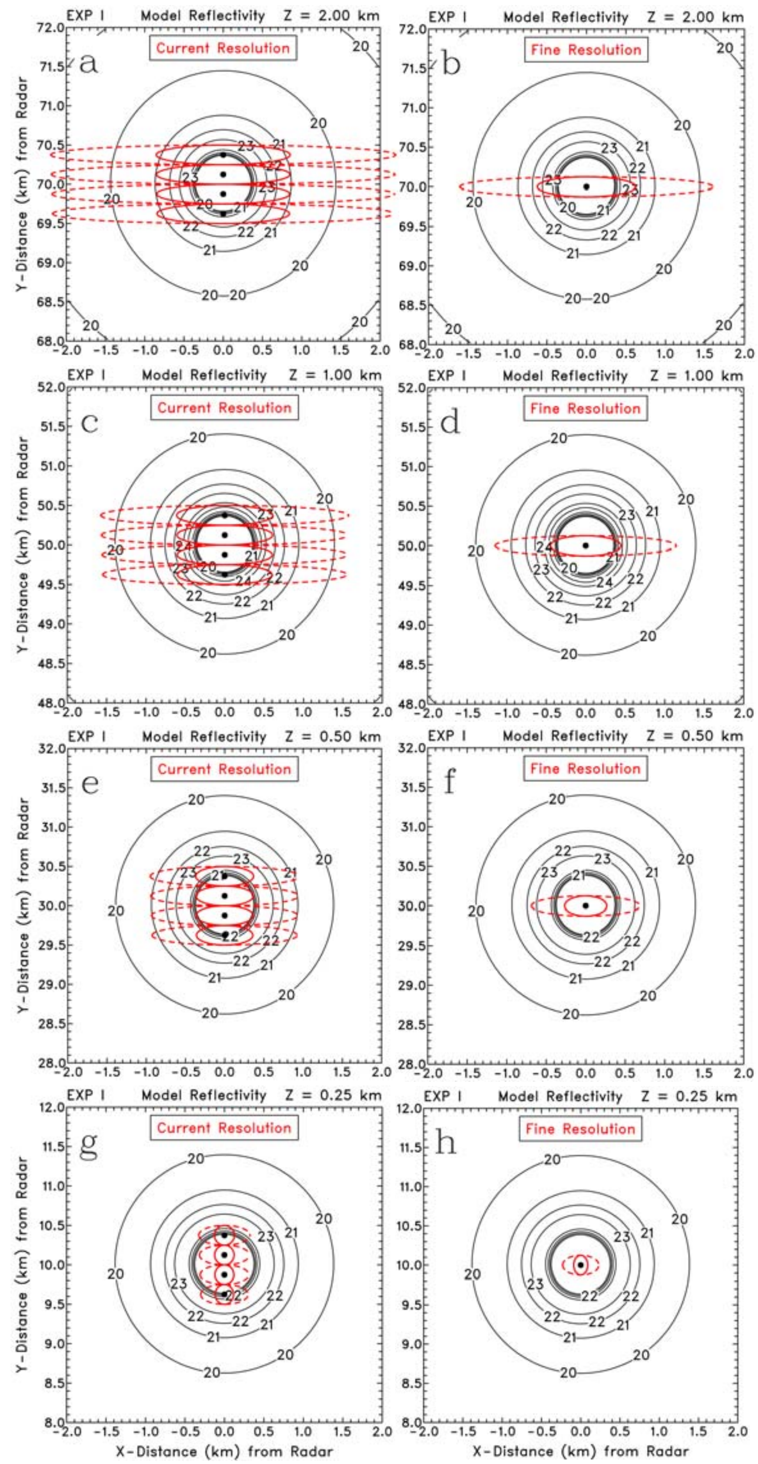

Fig. 3. Horizontal plots of superimposed effective half-power beamwidths (red, solid contours) and effective full beamwidth (red, dashed contours) on the model reflectivities (black, solid contours in dBZ) at heights of (a, b) 2.0 km, (c, d) 1.0 km, (e, f) 0.5 km and (g, h) 0.25 km for EXP I. Black dot represents the center of the sampling volume. Current-resolution data represent the average of four 0.25-km gates in range. The minimum model reflectivities are centered at 10, 30, 50 and 70 km from the radar. Only contours (black) $\geq$ 20 dBZ are indicated.

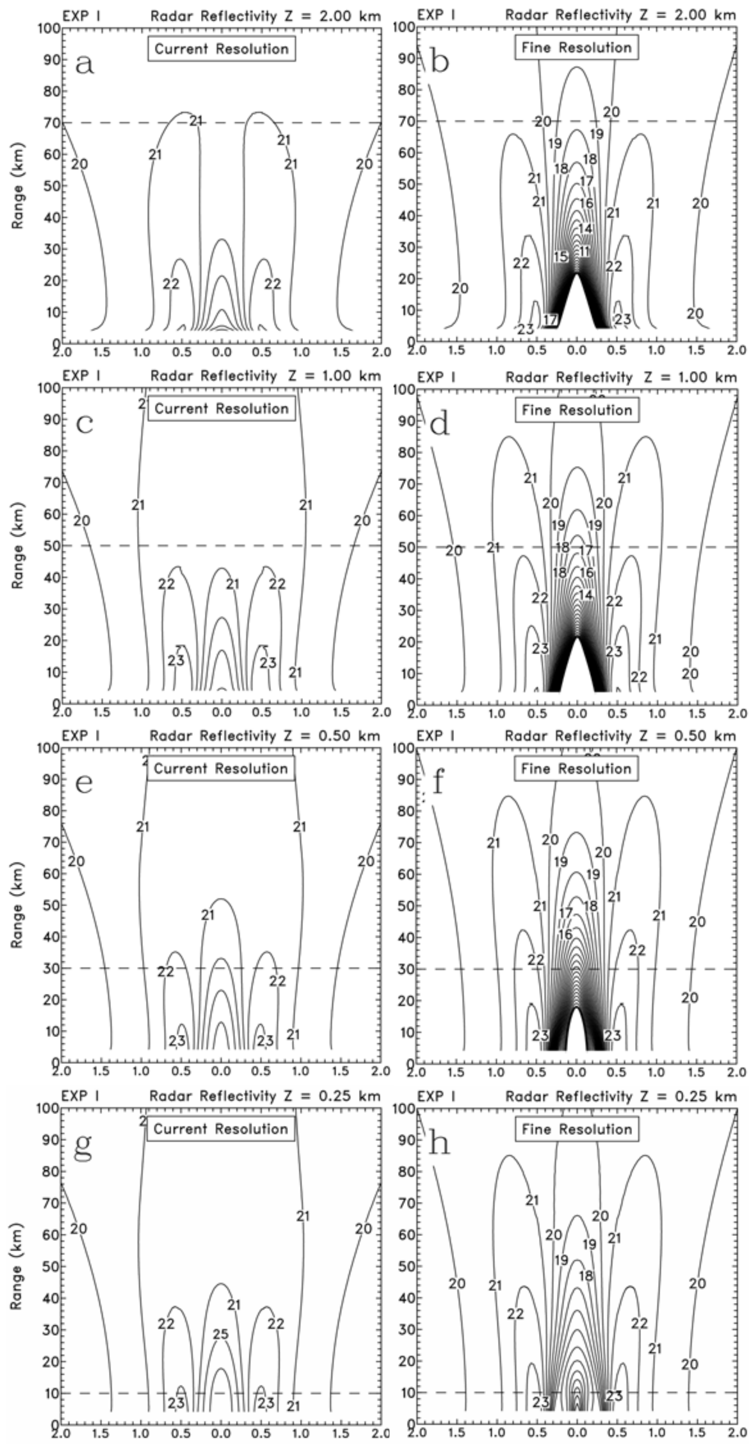

Fig. 4. Horizontal plots of current- and fine-resolution radar reflectivities scanned through the vortex centered at heights of (a, b) 2.0 km, (c, d) 1.0 km, (e, f) 0.5 km and (g, h) 0.25 km for EXP I. Current-resolution data represent the average of four 0.25-km gates in range. Only contours greater than 0 dBZ are indicated. Contours are based on data computed at 0.025-km intervals across the vortex center and 1.0-km intervals in range. Horizontal dashed lines correspond to ranges in Fig. 3.

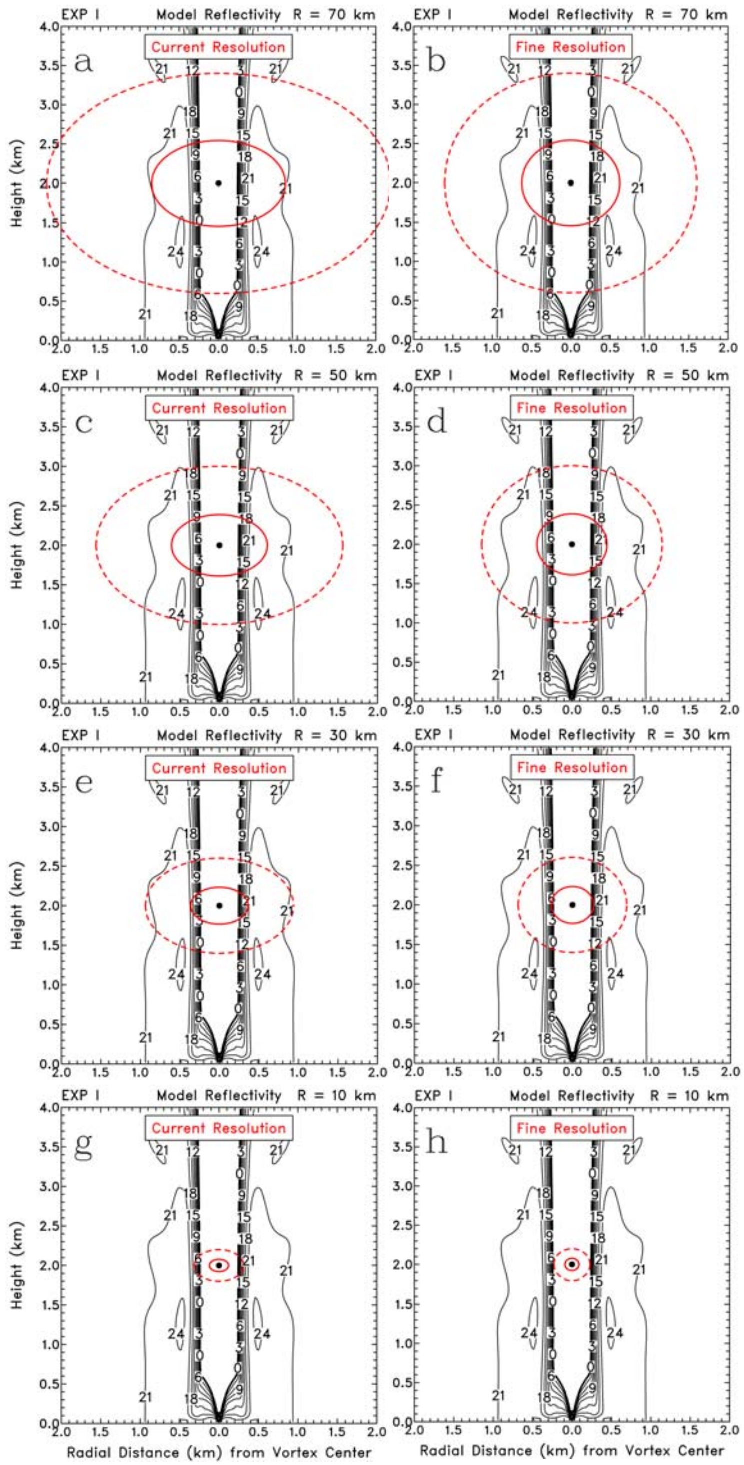

Fig. 5. Vertical plots of model reflectivity (black, solid contours in dBZ) superimposed with effective half-power beamwidth (red, solid contour) and effective full beamwidth (red, dashed contour) at ranges of (a, b) 70 km, (c, d) 50 km, (e, f) 30 km, and (g, h) 10 km from the radar. Black dot represents the center of the sampling volume.

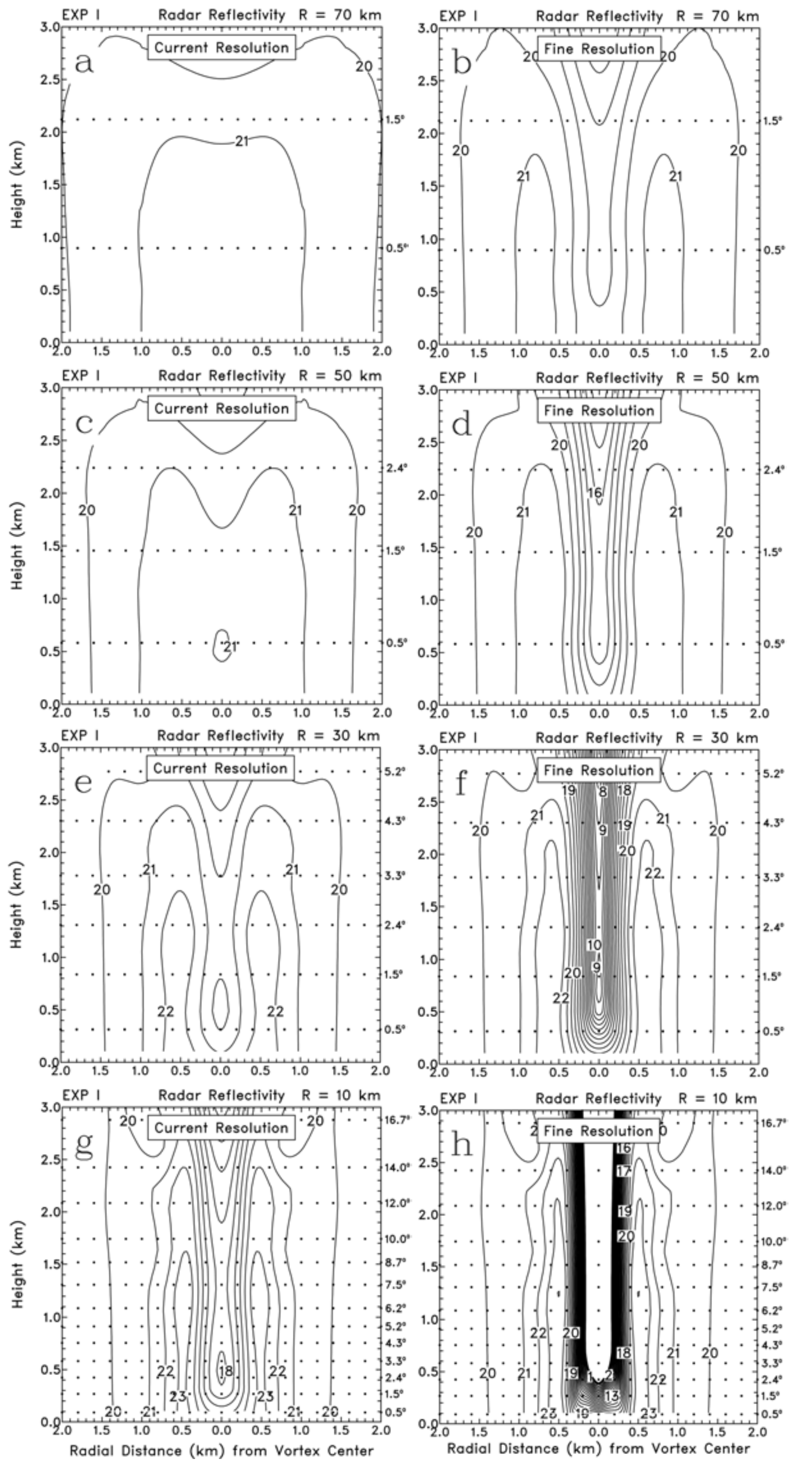

Fig. 6. Vertical plots of current- and fine-resolution radar reflectivities through vortex centered at ranges of (a)-(b) 70 km, (c)-(d) 50 km, (e)-(f) 30 km and (g)-(h) 10 km from the radar for EXP I. Current-resolution data represent the average of four 0.25-km gates in range. Only contours greater than 0 dBZ are indicated. Note that vertical dimension has been reduced from 4.0 km (Fig. 5) to 3.0 km to enlarge the details at the lowest few hundred meters. In each panel, dotted lines and values at the right side represent elevation angles of the WSR-88D Volume Coverage Pattern (VCP) 11.

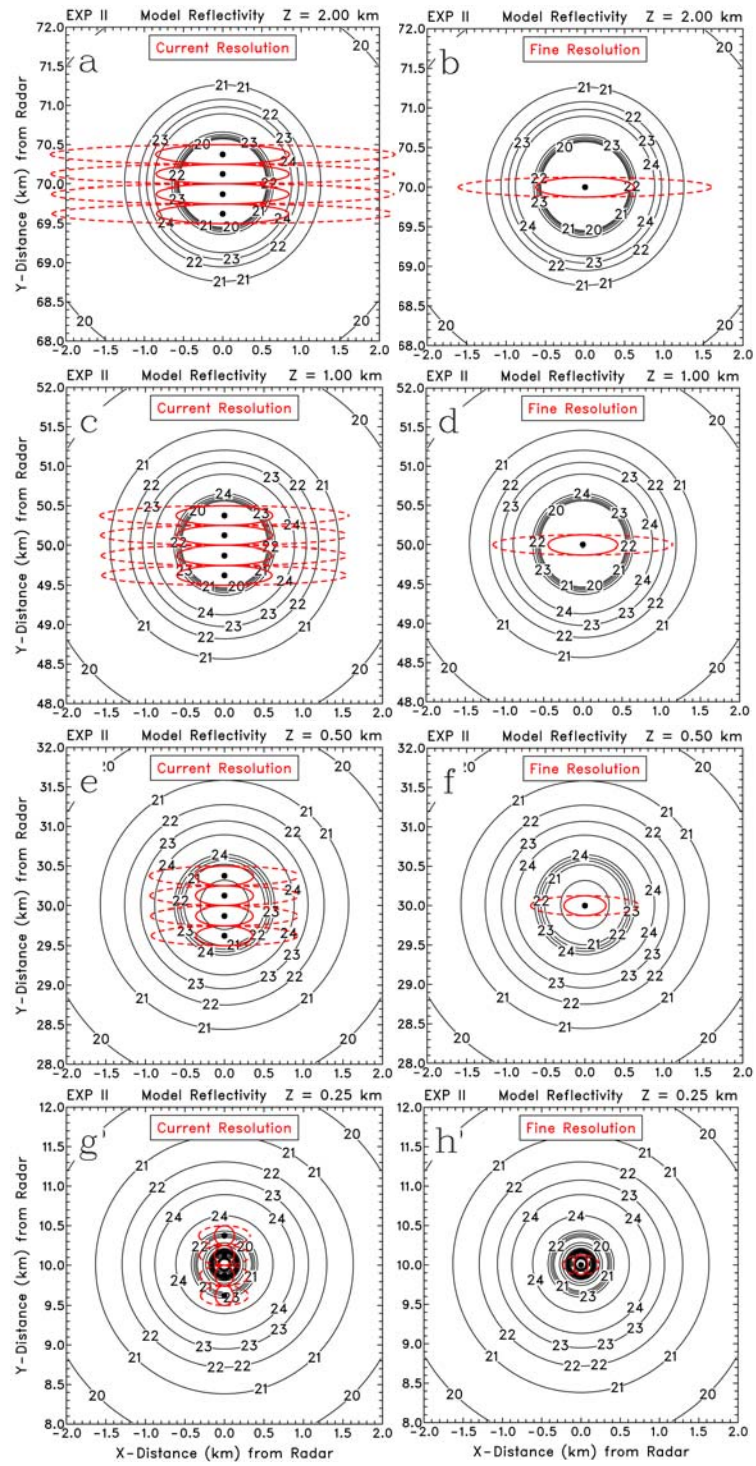

Fig. 7. Same as Fig. 3, except for EXP II.

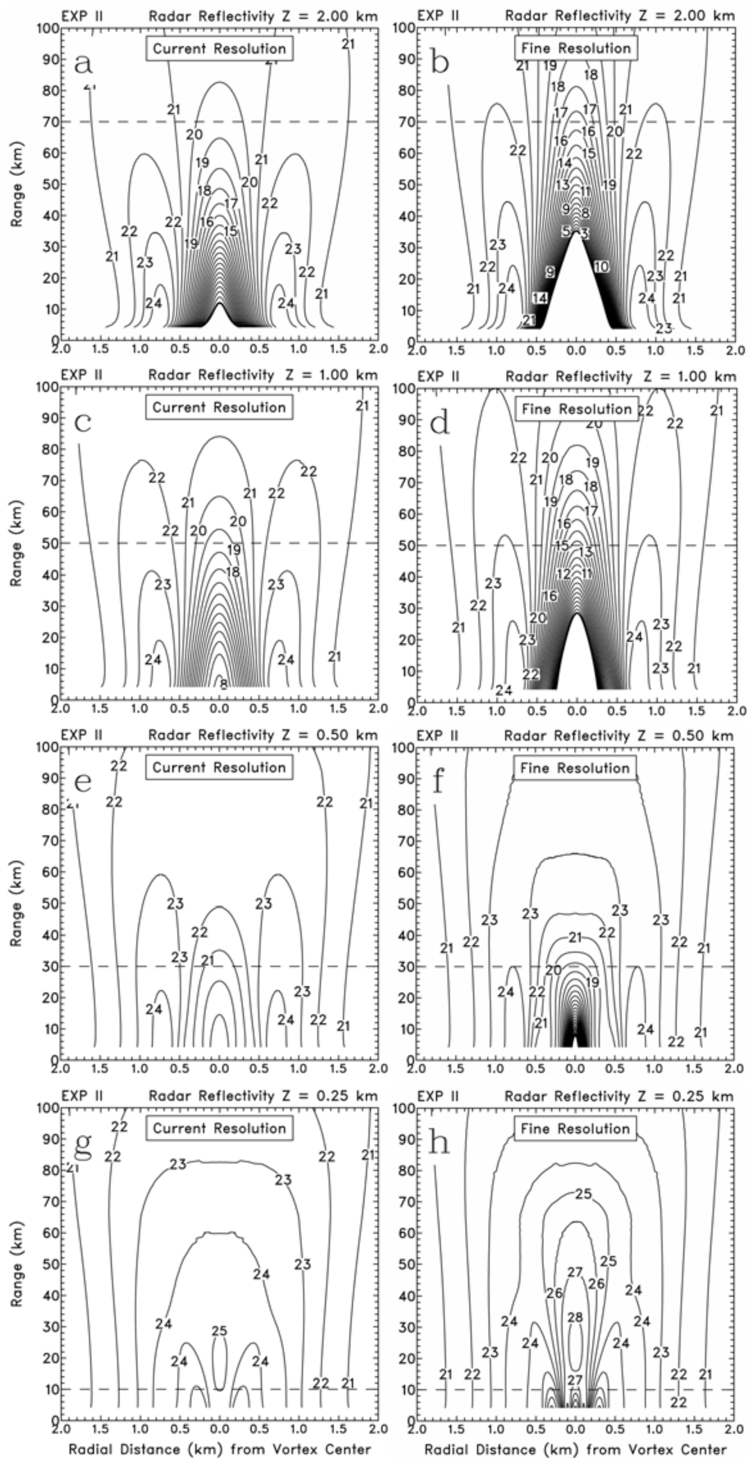

Fig. 8. Same as Fig. 4, except for EXP II.

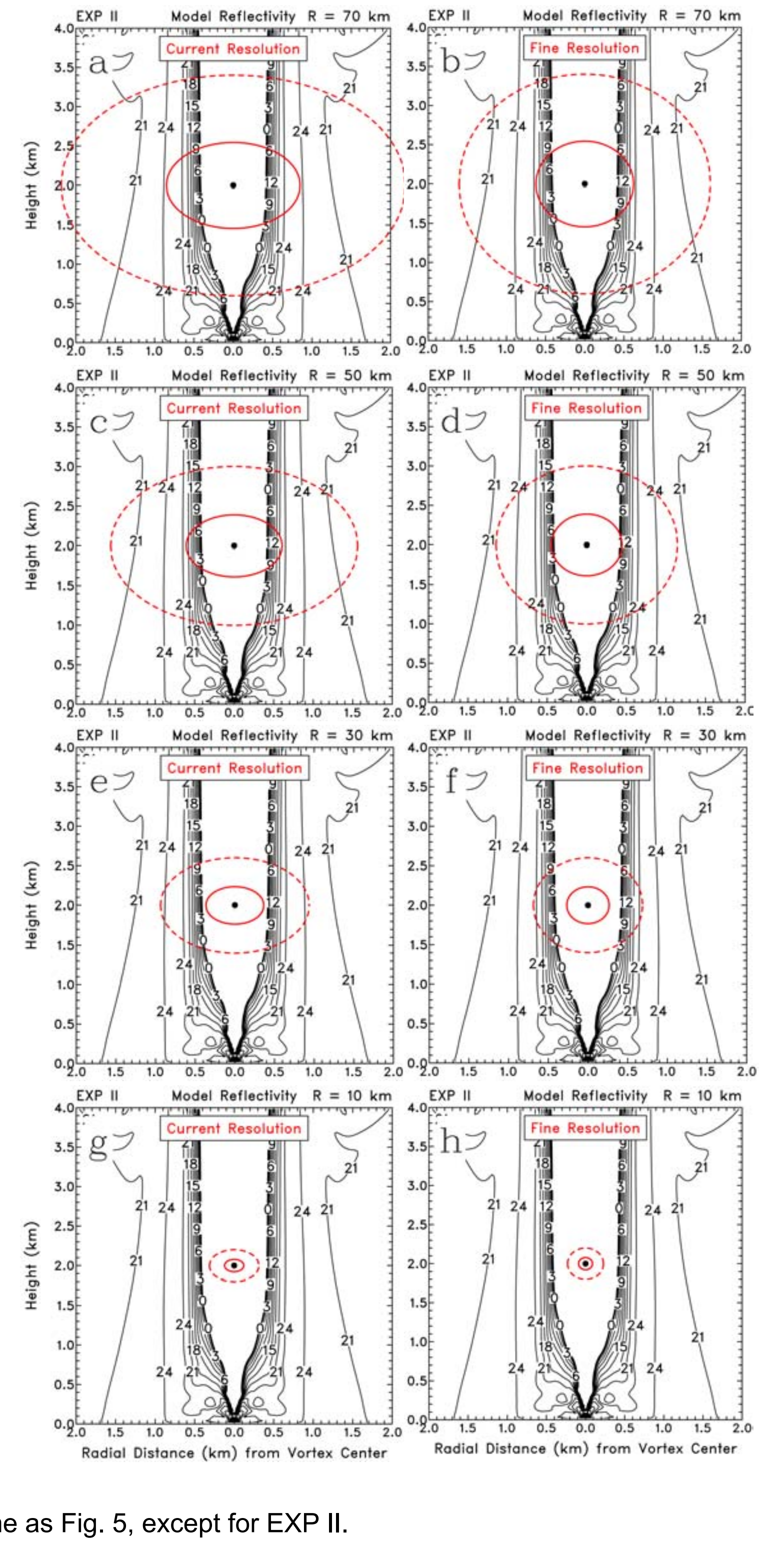

Fig. 9. Same as Fig. 5, except for EXP II.

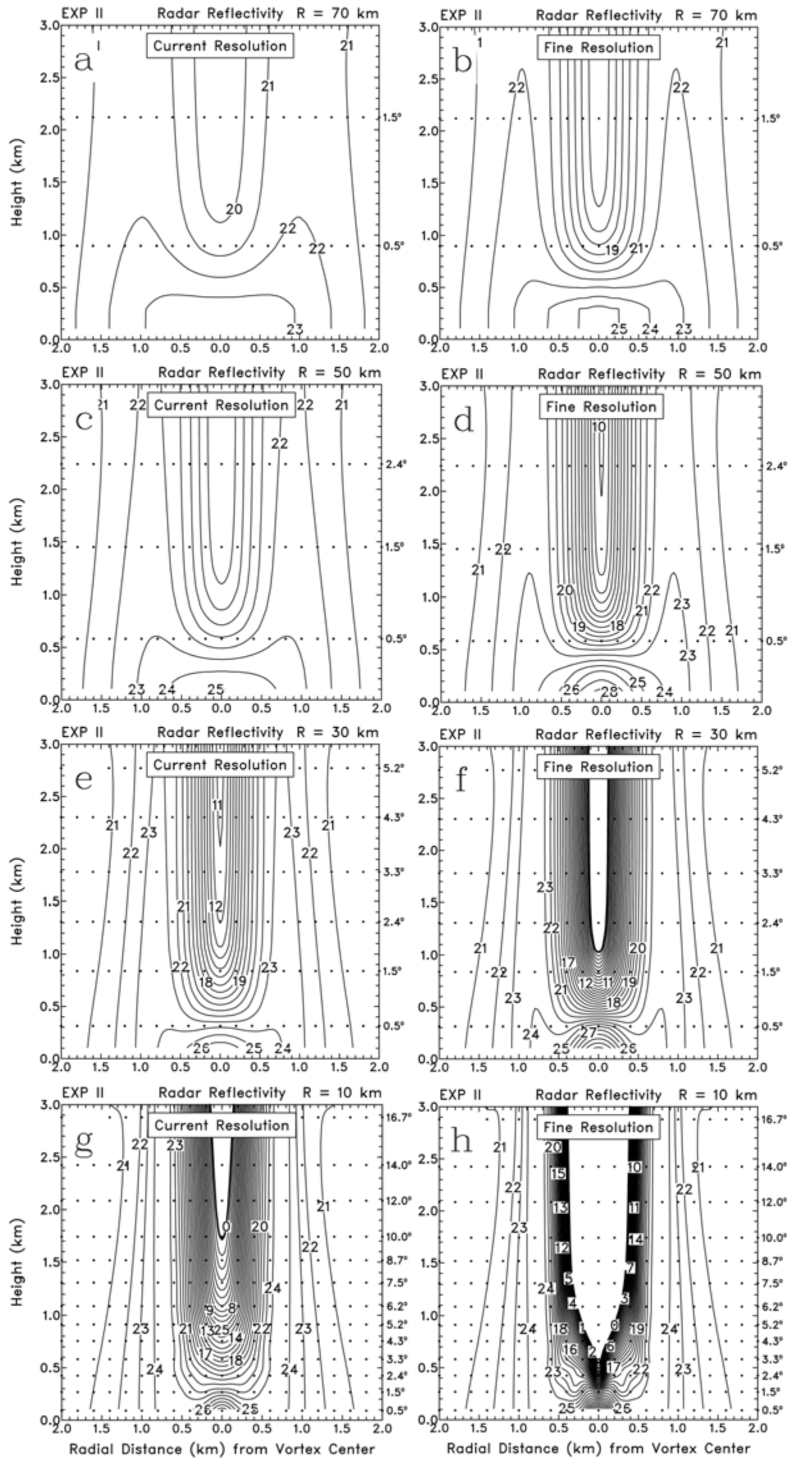

Fig. 10. Same as Fig. 6, except for EXP II.

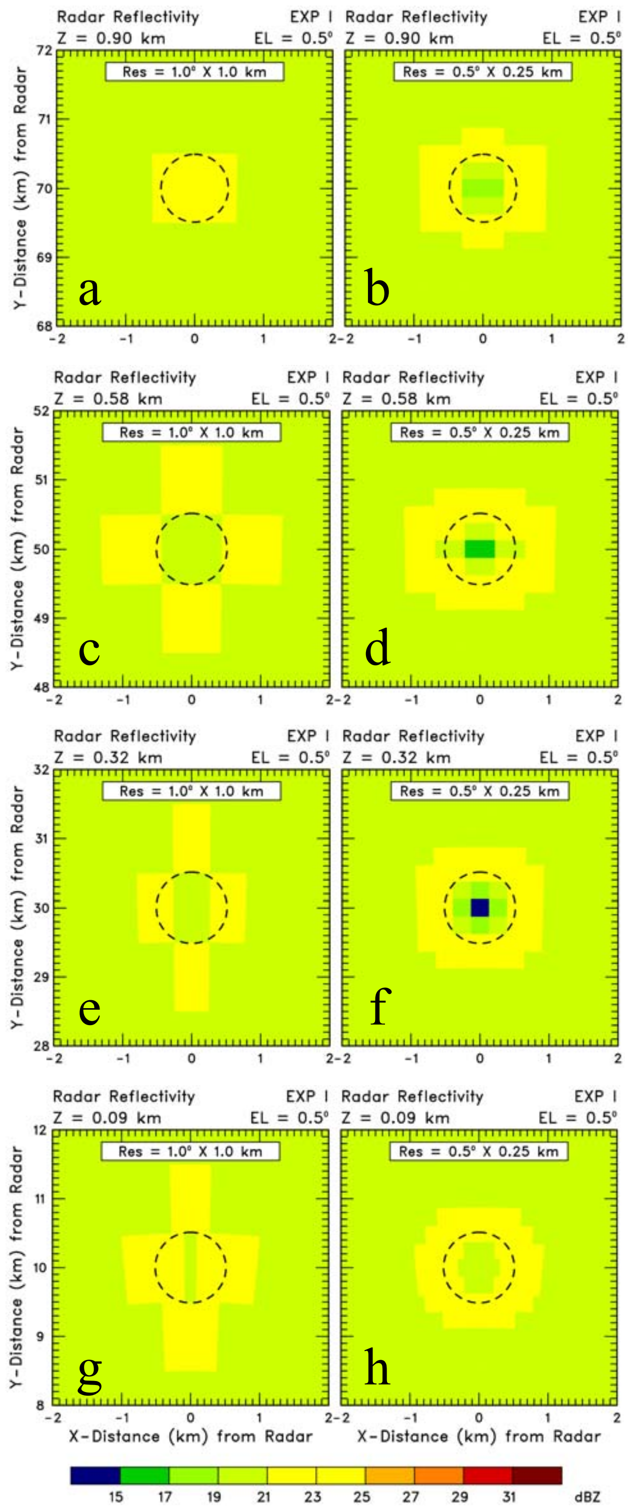

Fig. 11. Plan views of simulated Doppler radar reflectivity signatures measured by a radar located 10, 30, 50, and 70 km from a model low-reflectivity eye at 0.5° elevation angle for EXP I. In the left panels, current resolution is 1.0° azimuth by 1.0-km range. Fine resolution is 0.5° azimuth by 0.25-km range in the right panels. Dashed circle represents the true annulus of high reflectivities surrounding the low-reflectivity eye. Center heights are indicated. The radar is located beyond the bottom of the figure.

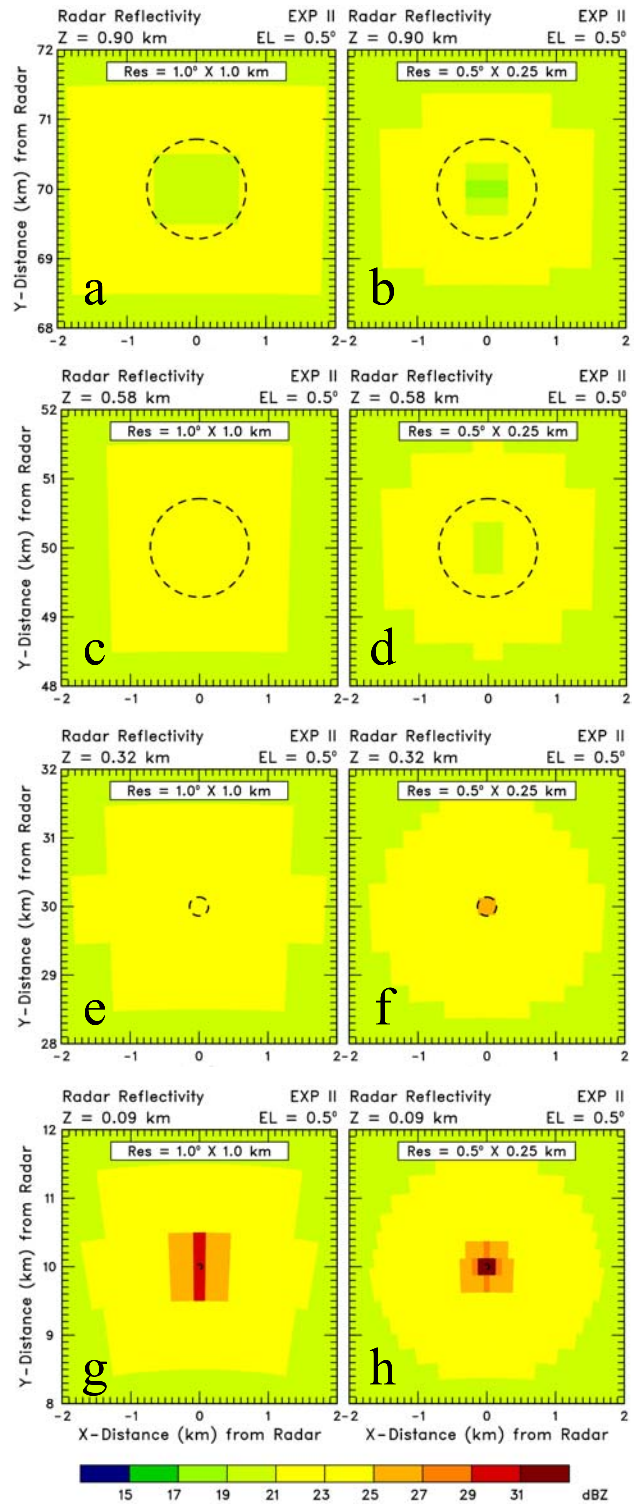

Fig. 12. Same as Fig. 11, except for EXP II.

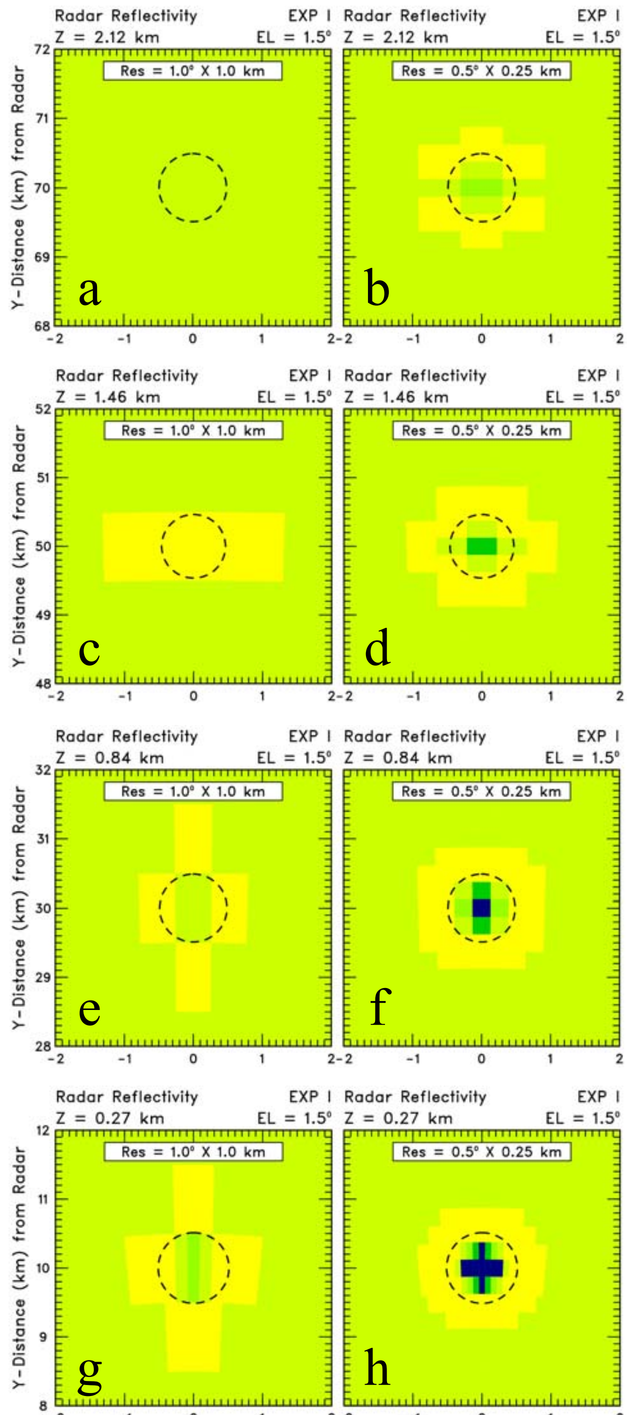

Fig. 13. Same as Fig. 11, except at 1.5° elevation angle.

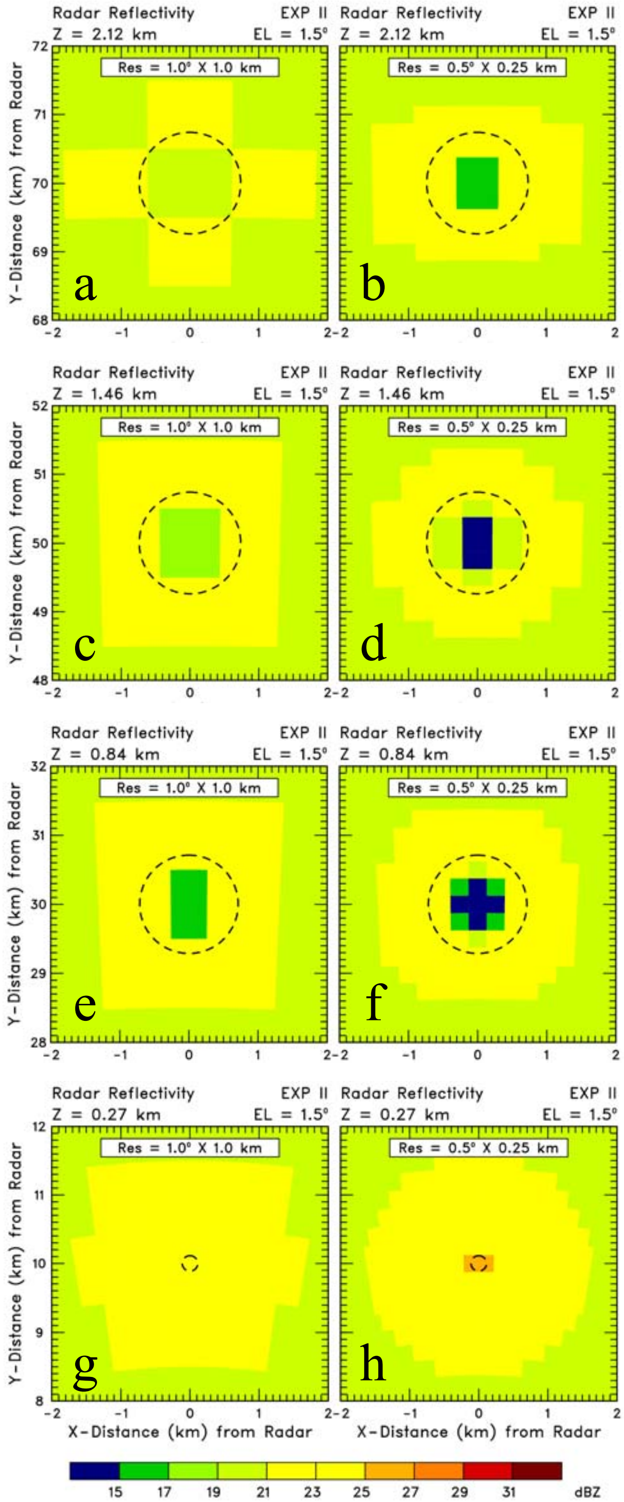

Fig. 14. Same as Fig. 13, except at 1.5° elevation angle.